



Band offset modulation in Si-EuO heterostructures via controlled interface formation

Wente Li , Agham B. Posadas, and Alexander A. Demkov ^{*}
Department of Physics, The University of Texas, Austin, Texas 78712, USA



(Received 6 July 2019; published 16 October 2019)

Combining first-principles calculations and experiment, we investigate the atomic and electronic structure of the Si/EuO interface. We consider the thermodynamic stability of interface structures with different levels of oxidation to identify the most probable configuration. By comparing the calculated band alignment and core-level shifts with measured values, we validate the theoretically constructed interface model. We find that the band offset can be tuned by altering the relative energy positions of the Si and EuO conduction bands via interface oxidation, which can be used to tune this materials system for specific applications in spintronics.

DOI: [10.1103/PhysRevB.100.155303](https://doi.org/10.1103/PhysRevB.100.155303)

I. INTRODUCTION

As continuing Moore's law scaling has become more and more challenging, the search for new means of information processing has intensified over the last two decades. Semiconductor-based spintronics is one such avenue. One of the best-known spintronic devices, a spin field-effect transistor (spin-FET), was suggested by Datta and Das as early as 1990 [1]. However, the practical implementation of their idea has proven to be quite difficult. The operation of a spin-FET consists of three major processes: generation and injection of spin-polarized electrons into the channel material, their transport, and spin manipulation with an external stimulus. In the original Datta-Das spin-FET a semiconductor was proposed as the channel to transport spin-polarized electrons, and ferromagnetic materials were used as source and drain. A heterojunction of a ferromagnetic metal and a semiconductor constitutes the spin injector component of a spin-FET. However, it was quickly realized that a conventional ferromagnetic metal–semiconductor contact would not work due to silicide formation reactions [2] and significant conductivity mismatch [3]. One way to resolve this problem is to introduce an insulating barrier layer between the semiconductor and metal to form a magnetic tunnel junction or MTJ [4]. Another way is to use a ferromagnetic semiconductor [5] to serve as a spin injector. Rocksalt EuO is a ferromagnetic semiconductor with a Curie temperature of 69 K [6], and with the fully spin-aligned Eu $4f$ states producing a tremendous $7 \mu_B$ magnetic moment per Eu [7]. The strong exchange interaction between the valence $4f$ states and the conduction-band Eu $5d$ states results in a very large conduction-band splitting of 0.6 eV between the spin-up and spin-down channels [5,8]. This large spin splitting makes doped EuO an excellent material for spintronic devices, albeit at low temperature. When doped n -type, e.g., by Gd, EuO shows 100% spin-polarized electrons in the $5d$ conduction band, while also having the benefit of being conductivity matched with Si. Another advantage of doping EuO is that doping increases the Curie temperature beyond

the boiling point of liquid nitrogen [9], making EuO much more practical for device applications. Alternatively, undoped EuO can also serve as a spin filter between a nonmagnetic metal and semiconductor in an MTJ-type arrangement, as an alternative means of injecting spin-polarized electrons into a semiconductor.

In a Si-based spintronic device, Si serves as the spin channel material. Owing to its small spin-orbit coupling, Si has a long spin relaxation lifetime and long spin coherence length, making it an excellent choice [10]. Because the rocksalt lattice of EuO is compatible with the fcc lattice of Si (see Fig. 1), and because EuO is thermodynamically stable on Si [5], Si/EuO heterostructures have a real potential for use in Si-based spin-FETs. Furthermore, it is worth pointing out that such a Si/EuO heterostructure would have a very high efficiency for spin injection because the momenta of electrons in EuO $5d$ and in the Si conduction band are matched well. We will discuss this point further in the following sections.

Several groups have proposed combining Si and EuO as a promising way to build a spin injector [5,8,11–19]. Schlom and co-workers reported that by using a SrO buffer layer one can prevent the chemical reaction between Eu metal and Si that results in the formation of metallic silicide EuSi_2 during EuO growth [15]. Caspers *et al.* reported another way to protect the Si surface by forming a monolayer of SiO_2 [16,17]. Both methods require the insertion of an insulating nonreactive buffer that in turn diminishes the spin injection efficiency. An alternative way to form EuO on Si is to use a Zintl layer of metallic Eu on Si, as reported by Caspers *et al.* [18] and Averyanov *et al.* [11–14]. Caspers *et al.* used x-ray photoemission spectroscopy (XPS) while Averyanov *et al.* used angle-resolved photoemission spectroscopy to investigate the electronic properties of the resulting interface structure. Both of these approaches essentially utilize the concept of a Zintl transition layer [20–23] that protects the highly active Si surface. They report a sharp Si/EuO interface without an amorphous interfacial layer [13].

Although several experimental reports of the Si/EuO growth and band structure have been published, very few papers discuss the relationship of the band alignment to spin injection. Depending on the magnitude and sign of the

^{*}demkov@physics.utexas.edu

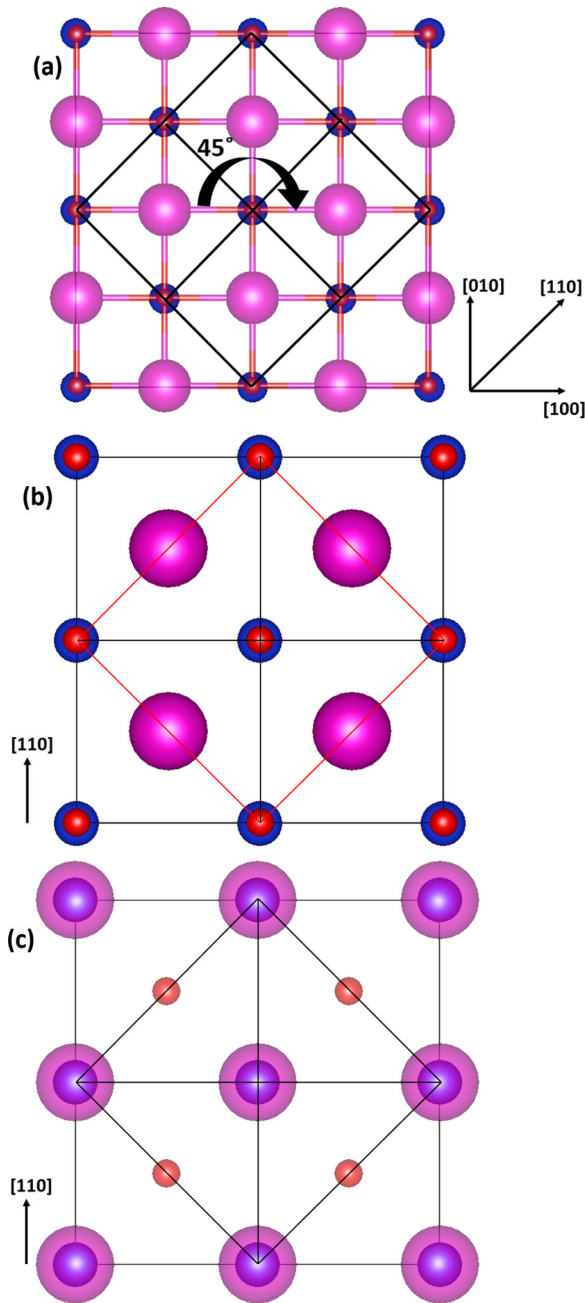


FIG. 1. (a) Top view of rocksalt EuO and face-centered silicon lattices. Purple ball represents Eu, red O, and blue Si. It can be seen that rocksalt and face-centered lattices match well. (b) rotates the structure in (a) by 45° . (b) Surface cell including two 2×1 silicon surface cells. (c) Surface cell showing an alternative matching approach compared with (b). We mainly focus on structure (b) because it is energetically favorable.

conduction-band offset (CBO), different implementations of spin injection may be accessible. If the conduction band of EuO is higher in energy than that of Si, the spin-polarized $5d$ conduction-band electrons in n -type EuO would result in direct spin injection into Si. On the other hand, if EuO is undoped, it could serve as a Schottky spin filter. If the conduction band of EuO is lower than that of Si, the spin

injection process could be modulated with an external electric field.

In this paper, we use a combination of first-principles theory and *in situ* XPS to study the electronic structure of the Si/EuO interface, specifically focusing on the relationship between the band alignment and the interface atomic structure. We determine theoretically the band alignment across the interface for different atomic arrangements and compositions and validate these models experimentally. To guide the EuO deposition, which is done using molecular-beam epitaxy (MBE), we investigate the thermodynamic stability of the interface with respect to possible interface chemical reactions. The rest of the paper is organized as follows. We briefly introduce the computational and experimental methods we use in Sec. II. In Sec. III, we describe building theoretically the Si/EuO interface and discuss the variety of interface atomic models that we considered along with their thermodynamic stability. We present the resulting band alignment and simulated XPS core-level shifts in Sec. IV. In Sec. V, we discuss our experimental results, and then we compare theory and experiment in Sec. VI. Section VII provides a summary of our results.

II. COMPUTATIONAL AND EXPERIMENTAL METHODOLOGY

We perform density-functional theory (DFT) calculations using the Vienna *Ab initio* Simulation Package (VASP) [24]. The generalized gradient approximation (GGA) [25] and projected-augmented-wave potentials [26] are employed. We use the valence configurations $3s^23p^2$ for silicon (Si), $5s^25p^64f^76s^2$ for europium (Eu), and $2s^22p^4$ for oxygen (O). In order to describe the highly localized Eu $4f$ states of EuO, we include the Hubbard-type U correction (GGA + U method) with $U = 8$ eV [27]. Integrals over the Brillouin zone are evaluated using the Monkhorst-Pack k -point meshes ($10 \times 5 \times 1$ for the Si/EuO heterostructure and $8 \times 8 \times 8$ for bulk Si and EuO). We use 500 eV as the cutoff energy. All structures are optimized with respect to the ionic positions until the forces are less than 20 meV/Å. We use the experimental lattice constant for Si of 5.43 Å (the DFT result is 5.46 Å, indicating only a 0.6% deviation). The calculated Si band gap is 0.58 eV, which is smaller than the experimental value of 1.12 eV and is typical of DFT calculations. The optimized lattice constant of bulk EuO is 5.186 Å, which agrees well with the previous theoretical results [27,28] and the experimental value of 5.14 Å. The EuO band gap between the spin-up Eu $4f$ and $5d$ states is 1.17 eV, in good agreement with previous calculations [27] and the experimental value of 1.12 eV. When considering the Si/EuO heterostructure, we consider Si as a substrate and strain EuO laterally to match it (see Fig. 1). This results in a 4.7% tensile epitaxial strain in EuO theoretically (it is 5.6% experimentally). The optimized, out-of-plane lattice constant of EuO is 5.07 Å, suggesting a Poisson ratio of 0.19, which is in good agreement with the value of 0.15 calculated by Ingle and Elfimov [29]. Strain results in the EuO band gap increasing to 1.26 eV. Accordingly, the energy difference between the valence-band top and the average electrostatic potential (needed in the band

alignment calculations discussed later) changes from 2.63 eV for unstrained EuO to 2.14 eV for the strained case.

When investigating the Si/EuO interface, we use a slab consisting of 6 EuO layers and 21 layers of Si. The slabs are separated by 12 Å of vacuum to avoid spurious interactions between them. We use the dipole correction to compensate for the field caused by the work function difference. We use a 2×1 lateral cell ($7.68 \text{ \AA} \times 3.84 \text{ \AA}$) of Si as a substrate. In a separate calculation of a Si slab of the same thickness, with a 2×1 reconstruction of the top surface and with the bottom surface passivated by hydrogen, we find a slightly wider band gap of 0.75 eV, compared to 0.58 eV for bulk Si. This gap opening is attributed to quantum confinement. It is worth pointing out that Bousquet *et al.* [30] have reported ferroelectricity in strained EuO. As the polarization field may influence the band alignment, the effect warrants careful consideration and will be discussed further later.

For the experimental deposition of EuO on Si, we take lightly doped *n*-type Si(100) wafers that have been diced into 20 mm squares as the substrate. The Si is degreased in acetone, isopropanol, and deionized water with sonication for 5 min each. The substrate is then exposed to UV/ozone for 15 min to remove carbon contaminants from the surface. The Si substrates are then loaded into the MBE deposition chamber for EuO growth. Prior to EuO deposition, the native SiO₂ layer is removed using a variant of the Sr-assisted deoxidation process [22], using Eu metal instead of Sr metal. The Eu metal is evaporated from an effusion cell operated at $\sim 530 \text{ }^\circ\text{C}$ producing a metal flux of 1 monolayer per minute, defined as 1 Eu atom per Si atom on the Si(100) surface. After outgassing the substrate at $700 \text{ }^\circ\text{C}$ for 10 min, 3 monolayers of Eu metal are deposited causing EuO and SiO to form on the surface, with any excess Eu metal evaporating away. The substrate is then heated to $850 \text{ }^\circ\text{C}$, upon which SiO becomes volatile and desorbs, while also slowly vaporizing the small amount of EuO remaining. After a clear 2×1 reconstruction of the Si surface is observed by reflection high-energy electron diffraction (RHEED), the substrate is kept at $850 \text{ }^\circ\text{C}$ for 15 min to fully remove any Eu or SiO_x, before the substrate is cooled down to $600 \text{ }^\circ\text{C}$. At this temperature, 1/2 monolayer of Eu metal is deposited, which bonds to the reconstructed Si surface to form the 1/2 monolayer Eu Zintl layer. The substrate is then cooled down to $200 \text{ }^\circ\text{C}$ for EuO deposition. Figure 2(a) shows the RHEED pattern of 1/2 monolayer Eu on Si, showing a 2×1 reconstruction along Si[110].

EuO deposition on Si is accomplished using two different pathways. The first pathway takes the 1/2 monolayer Zintl template surface and exposes it to oxygen at 3×10^{-9} Torr partial pressure. After about 5 min, the Eu shutter is opened and EuO starts forming on the surface as confirmed by RHEED. Immediately after the shutter is opened, the substrate temperature is ramped to $350 \text{ }^\circ\text{C}$ (at a rate of $20 \text{ }^\circ\text{C}/\text{min}$) while the EuO is depositing until 2.5 nm of EuO has been deposited (10 min growth time). Figure 2(b) shows the RHEED pattern of EuO grown using the first pathway. The second pathway starts from the 1/2 monolayer Zintl template surface and then an additional 1/2 monolayer of Eu metal is deposited at $200 \text{ }^\circ\text{C}$, resulting in a transition from $2 \times$ to $3 \times$ surface reconstruction as observed by RHEED and shown in Fig. 2(c). Oxygen is then let into the deposition chamber to a partial

pressure of 3×10^{-9} Torr as in the first pathway and then the Eu shutter is reopened to form EuO. The substrate temperature is ramped to $350 \text{ }^\circ\text{C}$ as above and EuO is grown to a thickness of 2.5 nm. Figure 2(d) shows the RHEED pattern of EuO grown using the second pathway. Immediately after growth, the samples are transferred in vacuum to an *in situ* XPS analysis chamber with a VG Scienta R3000 analyzer and monochromated Al K α x-ray source. The Eu 3*d*, Eu 4*d*, O 1*s*, Si 2*p*, and valence band of the samples are measured. The analyzer is calibrated such that the Ag 3*d*_{5/2} level of a clean Ag surface is at a binding energy of 368.28 eV.

III. INTERFACE MODEL CONSTRUCTION AND THERMODYNAMIC STABILITY STUDY

Firstly, we describe how we build atomistic models of the Si/EuO interface. We start by considering 1/2 monolayer (ML) of Eu on the 2×1 -reconstructed (001) Si surface. The previous work on Sr and Ba on the 2×1 -reconstructed Si and Ge (001) surface [23,31–33] suggests that such a layer (known as Zintl layer due to stoichiometric similarity to the intermetallic silicide) provides a template for the subsequent epitaxial oxide growth, while protecting Si from oxidation [23]. A similar mechanism has been proposed for growing EuO on Si [12].

To identify the most energetically favorable positions of Eu adatoms on the Si surface, we calculate the potential-energy surface (PES) as shown in Fig. 3(a). We divide the surface simulation cell into a 9×5 grid and calculate the total energy after placing one Eu adatom at each grid point. During the structural optimization, we freeze the lateral motion of Eu allowing it to move only in the *z* direction, while all other atoms are free to move. We find that, similar to Sr on Si (001), the minimum energy sites are in the trough, between the Si dimers. The maximum energy point is above the dimerized Si atom, and the lowest energy site is 2.1 eV lower than the maximum energy site. By using climbing nudged elastic band (cNEB) method [34], the energy barrier for Eu adatom diffusion along the [110] direction to the next minimum point is 1.0 eV, while it is 1.2 eV along the $[-110]$ direction. The ball and stick model of the 1/2 ML Eu Zintl template is shown in Fig. 3(b). By using the equation $\Gamma = \nu e^{-E/k_B T}$, where ν is the attempt frequency (approximated as vibrational frequency $\nu = \frac{1}{2\pi} \sqrt{\frac{k}{m}}$ of Eu adatom [35] where *k* is the spring constant in the direction of diffusion and *m* is the mass of the Eu adatom), *E* is the energy barrier for the Eu adatom hopping between each most stable site, *k_B* is the Boltzmann constant, and *T* is temperature, we can estimate the diffusion rate Γ for a Eu adatom on the Si surface along the [110] and $[-110]$ directions. Comparing to the results of Sr and Ba adatom diffusion on the Si surface reported by Refs. [23] and [35], we summarize all results in Table I and note that the diffusion rate of Eu is smaller than that of Sr and Ba, especially along the [110] direction.

Next, we add six layers of EuO atop this template. To match the 2×1 cell of Si, we rotate the conventional rocksalt cell of EuO by 45° (the schematic of the lattice matching is shown in Fig. 1). There are two options to place rocksalt EuO on top of the 1/2 ML Eu Zintl template: (1) oxygen atom

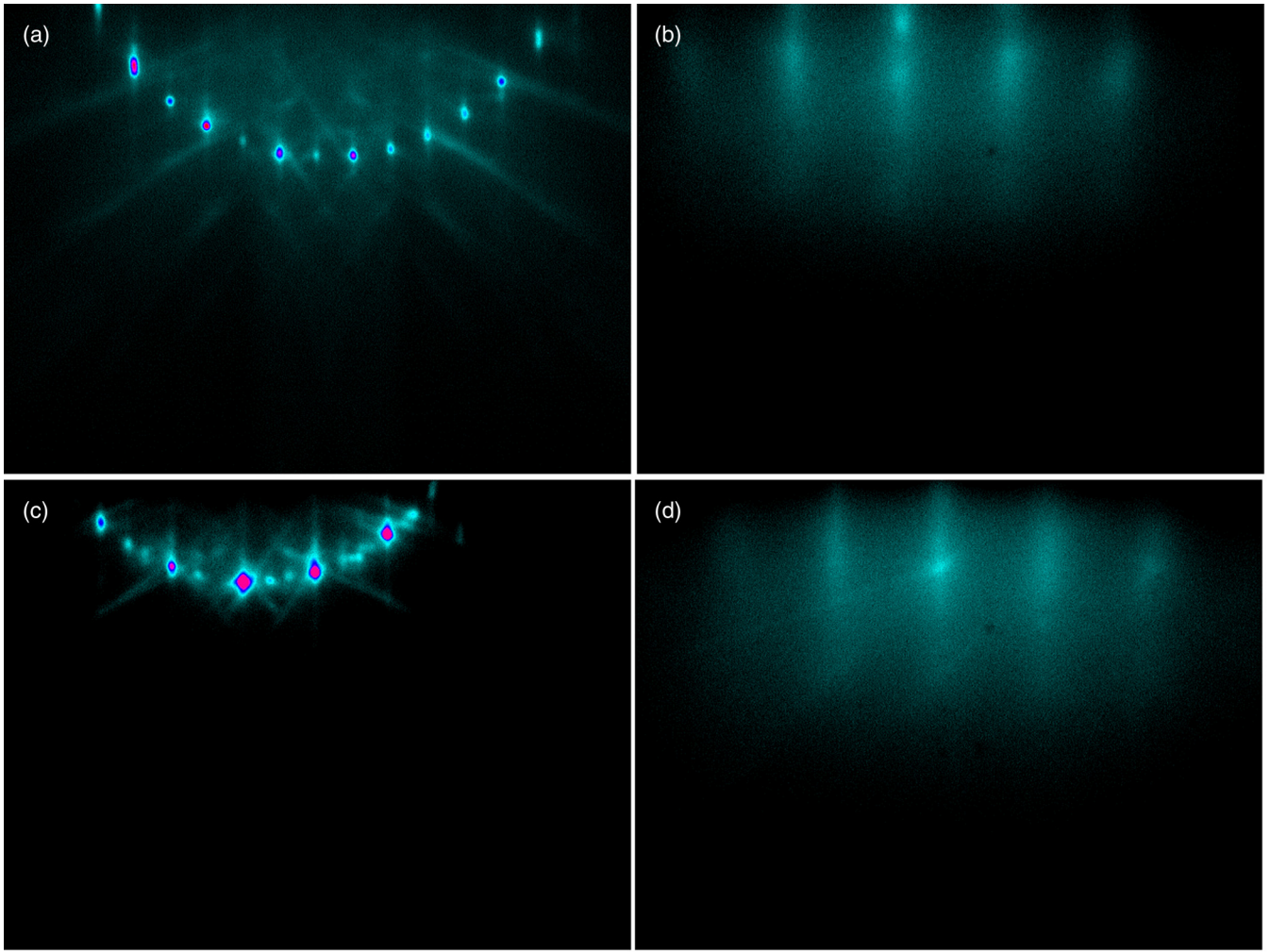


FIG. 2. RHEED patterns of Eu and EuO on Si(100) viewed along Si[011] azimuth. (a) $2\times$ reconstruction observed after depositing $1/2$ ML Eu on Si at 650 °C. (b) EuO on Si grown using the oxygen-first method. (c) $3\times$ reconstruction observed after 1 ML of Eu metal deposited on Si at 200 °C. (d) EuO on Si grown using the metal-first method.

directly above the Eu atom of the template [Fig. 1(b)], and (2) Eu atom in EuO directly above the Eu atom of the template [Fig. 1(c)]. The former configuration is 1.75 eV more stable than the latter, and in the following discussion we will assume the former configuration is preferred and focus only on such interfaces. It is well known that oxidation of Si dimers at the interface will influence the interface electronic structure and band alignment [23,31,33]. Therefore, we vary the number of interface oxygen atoms to simulate different oxidization

conditions. When oxygen inserts itself in the dimer, we call this a bridging oxygen (b. oxygen); another configuration called decorating oxygen (d. oxygen) is when oxygen attaches to the dimer dangling bond. In total, we have considered 6 different interface models as shown in Figs. 4(a)–4(f), arranged in order of increasing interfacial oxygen content from zero to 2 per simulation cell.

It is important to identify which interface is most energetically favorable under different chemical conditions. Because

TABLE I. Diffusion rates of Eu, Sr [23], and Ba [34] adatom on Si (001) 2×1 -reconstructed surface. “Ratio” is ratio of diffusion rate along $[110]/[-110]$.

Diffusion direction	Green line in Fig. 3(a) [110]			Blue line in Fig. 3(a) [-110]		
	Eu	Sr [23]	Ba [34]	Eu	Sr [23]	Ba [34]
Energy barrier (eV)	1.00	0.398	0.95	1.20	1.092	1.39
Spring constant ($\text{eV}/\text{\AA}^2$)	0.98	N/A	0.92	1.02	N/A	1.20
Attempt frequency (Hz)	1.25×10^{12}	10^{12}	N/A	1.28×10^{12}	10^{12}	N/A
Diffusion rate (Hz) (300 K)	3.02×10^{-5}	10^3	N/A	1.36×10^{-8}	10^{-7}	N/A
	Ratio: 10^{13}	Ratio: 10^{10}	Ratio: 2×10^7			

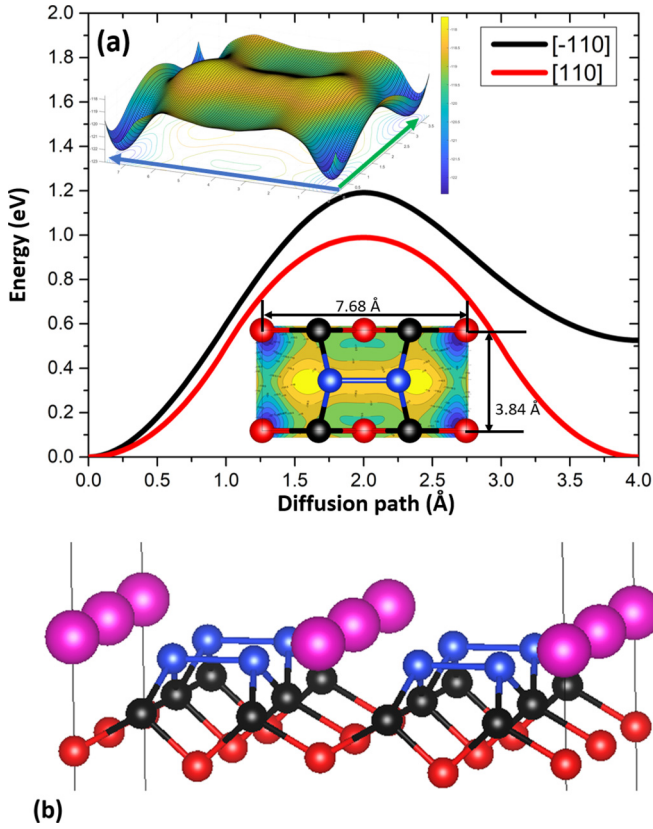


FIG. 3. (a) cNEB energy barrier profile along the [110] and $[-110]$ diffusion paths. The upper inset panel is PES of Eu adatom on top of 2×1 silicon surface (7.68×3.84 Å). Blue arrow indicates the diffusion path between the two nearest most stable sites of Eu adatom along the $[-110]$ direction and the green one indicates the path along the [110] direction. The lower inset panel is the contour plot of PES and relative position of Si atoms. (b) Ball and stick model of the most stable Eu Zintl layer. Blue balls represent first layer Si, black second, and red third. Purple balls represent Eu atoms.

the total number of atoms varies between the interface models, to compare them we use interface free energy defined as

$$F = E_{\text{slab}} - E_{\text{surface}} - (m_1 \tilde{\mu}_{\text{EuO}} + m_2 \tilde{\mu}_{\text{Si}}) - \left(m_3 \tilde{\mu}_{\text{Eu}} + \frac{m_4}{2} \tilde{\mu}_{\text{O}_2} + m_5 \tilde{\mu}_{\text{Si}} \right), \quad (1)$$

where E_{slab} is the energy of the simulation cell, E_{surface} is the surface energy of EuO and H-passivated Si, and m is the number of formula units of each component. The total energy of the slab consists of three parts: surface energy, interface energy, and bulk energy of all formula units. The chemical potential $\tilde{\mu}_a$ is defined as $\tilde{\mu}_a = \mu_a + E_a$, where μ_a is the chemical potential of element a (EuO, Si, Eu, or O_2) and E_a is its bulk energy. We divide the simulation cell into three parts along the direction normal to the interface: the surface, bulk [terms in the first bracket of Eq. (1)] and interface regions [terms in the second bracket of Eq. (1)] as shown in Fig. 5(a). For the bulk region, we define $\tilde{\mu}_{\text{EuO}} = E_{\text{EuO}}$ and $\tilde{\mu}_{\text{Si}} = E_{\text{Si}}$. In the interface region, we can potentially have the following chemical reactions:

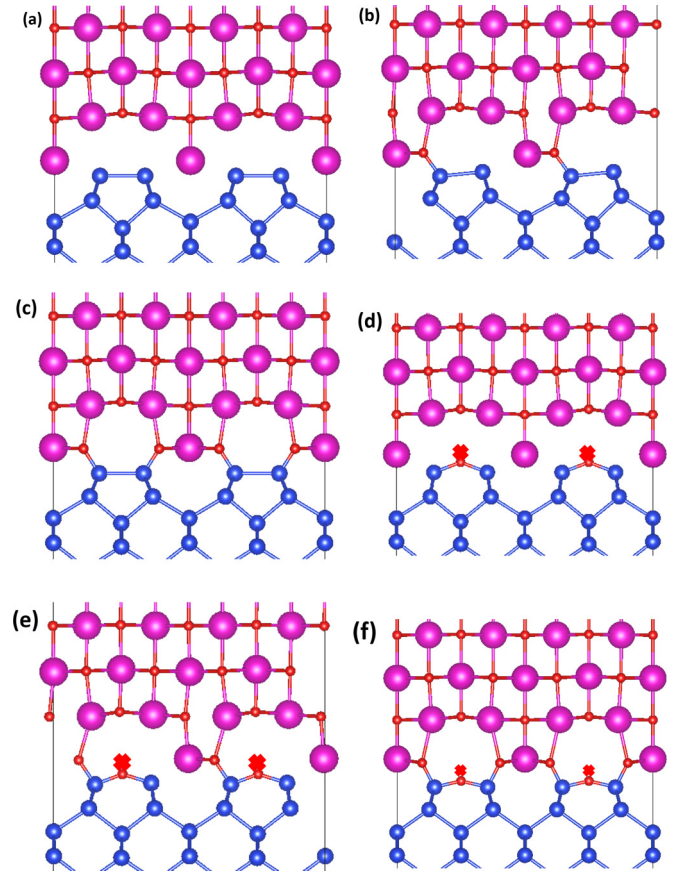
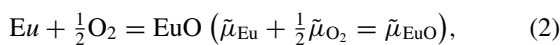
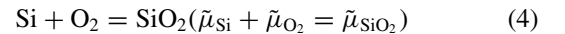
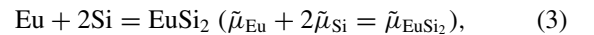
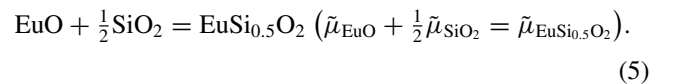


FIG. 4. Interface atomic structure of different interface models. Blue balls represent Si, red O, and purple Eu. Bridging oxygen atoms are labeled by red crosses. (a) Interface model I with 0 b. oxygen and 0 d. oxygen. (b) Interface model II with 0 b. oxygen and 1 d. oxygen. (c) Interface model III with 0 b. oxygen and 2 d. oxygen. (d) Interface model IV with 1 b. oxygen and 0 d. oxygen. (e) Interface model V with 1 b. oxygen and 1 d. oxygen. (f) Interface model VI with 1 b. oxygen and 2 d. oxygen.



and



Based on the atomic and electronic structures of all six interface models, we define the region between the 19th Si layer and the 2nd EuO layer as the interface region for interface models I, III, IV, and VI, and between the 19th Si layer and the 3rd EuO layer for interface models II and V. In the actual experiment, the presence of the Si substrate creates Si-rich conditions, so we can merge $m_5 \tilde{\mu}_{\text{Si}}$ into the first bracket in Eq. (1). We are left with two free variables (the chemical potentials $\tilde{\mu}_{\text{Eu}}$ and $\tilde{\mu}_{\text{O}_2}$) in the interface term [second bracket in Eq. (1)]. We have the following relations based on the equilibrium conditions [Eqs. (2)–(5)]: $\max(E_{f,\text{EuSi}_2}, E_{f,\text{EuO}}, E_{f,\text{EuSi}_{0.5}\text{O}_2}) \leq$

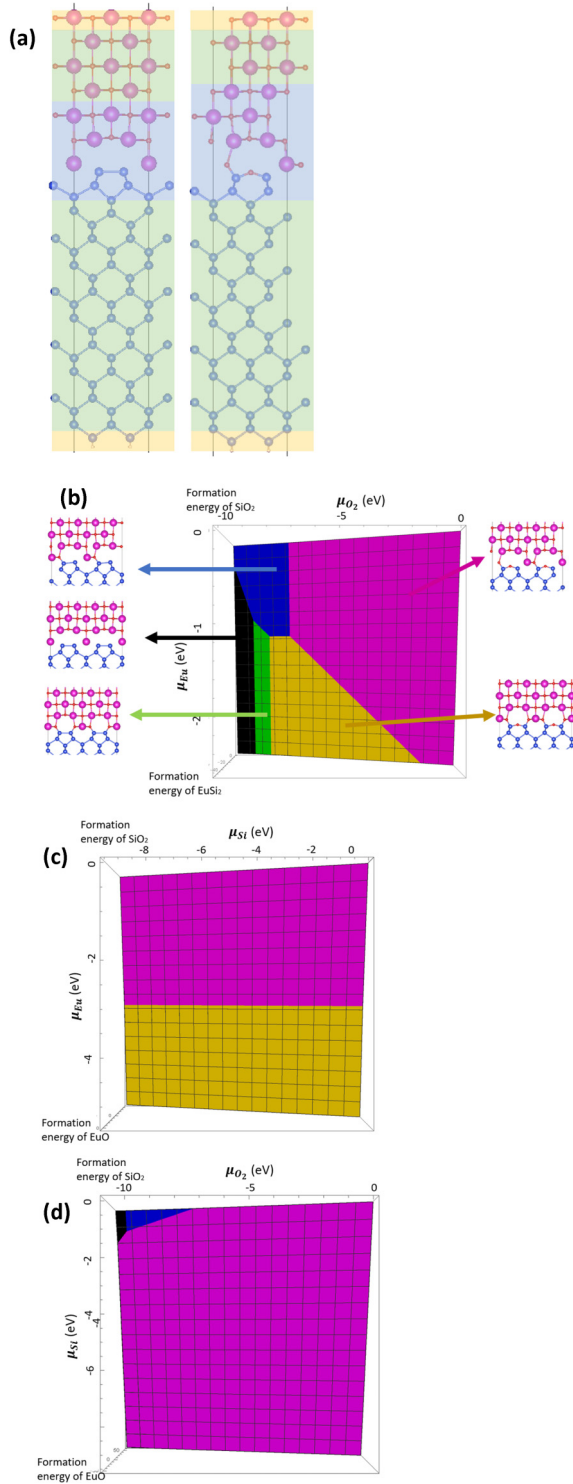


FIG. 5. (a) Schematic of the different regions of the heterostructure: yellow represents the surface region; green represents the bulk region; and blue represents the interface region. Interface models I, III, IV, and VI follow the scheme shown in the left panel (model III shown as an example), while models II and V follow the scheme shown in the right panel (model V shown as an example). (b) Phase diagram for experimentally relevant Si-rich conditions. Color representations of the six interface models are indicated by the color arrows. (c) Phase diagram for O-rich conditions. (d) Phase diagram for Eu-rich conditions. The color scheme used in (b) is also used in (c) and (d).

$\mu_{\text{Eu}} \leq 0$, where E_{f,EuSi_2} , $E_{f,\text{EuO}}$, and $E_{f,\text{EuSi}_{0.5}\text{O}_2}$ are the formation energies of EuSi_2 , EuO , and $\text{EuSi}_{0.5}\text{O}_2$, and $\max(E_{f,\text{EuO}}, \frac{1}{2}E_{f,\text{EuSi}_{0.5}\text{O}_2}) \leq \frac{1}{2}\mu_{\text{O}_2} \leq 0$, where E_{f,SiO_2} is the formation energy of SiO_2 .

Theoretical formation energies are $E_{f,\text{EuSi}_2} = -2.60$ eV, $E_{f,\text{EuO}} = -5.34$ eV, $E_{f,\text{EuSi}_{0.5}\text{O}_2} = -11.79$ eV, and $E_{f,\text{SiO}_2} = -9.45$ eV. We now can calculate the interface free energy for all six models and determine the most stable one under specific conditions (μ_{Eu} , μ_{O_2}), which yields a two-dimensional phase diagram shown in Fig. 5(b). These phases represent the most stable interface model (the lowest plane in this region of chemical potential).

The oxygen incorporation at the BaO/Si interface, which has the same atomic structure as our model, has also been studied by other researchers [33,36,37]. By combing synchrotron measurements and first-principle calculations, the authors of Ref. [36] report that 1 ML of O bonded to Si exists at the BaO/Si interface, which is similar to our structure III. The authors of Ref. [37] conclude that more oxygen atoms should be involved in a realistic interface. This is in line with our model VI, in which one extra bridging oxygen (incorporated into the Si dimer) is present, in addition to the two decorating oxygen atoms.

We also plot the phase diagrams for the Eu-rich conditions (free variables μ_{O_2} , μ_{Si} ; $\tilde{\mu}_{\text{Eu}} = E_{\text{Eu}}$) in Fig. 5(c), and for oxygen-rich conditions (free variables μ_{Eu} , μ_{Si} ; $\tilde{\mu}_{\text{O}_2} = E_{\text{O}_2}$) in Fig. 5(d). All three phase diagrams agree with each other well, which indicates that the chemical potential of oxygen controls the interface oxidation and that of europium can influence the number of decorating oxygen atoms, while Si only has a small effect in the oxygen-rich case but influences interface oxygen in the Eu-rich case.

IV. THEORETICAL BAND ALIGNMENT AND CORE-LEVEL SHIFTS

Due to the well-known problem in the theory of poorly predicting the energy of unoccupied states, to estimate the conduction band offset we calculate the valence-band offset (VBO) first and use experimental values for the band gaps of Si and EuO to obtain the CBO. To estimate the VBO, we use both the average potential method (APM) [38] and projected density of states (PDOS) analysis. To illustrate our approach, we shall use the interface shown in Fig. 4(c) (interface model III with zero bridging O and two decorating O) as an example. Using the APM, we plot the local electrostatic potential $V(z)$ along the direction normal to the interface (the z direction) of the simulation cell [the black line in Fig. 6(a)] and calculate the macroscopically averaged electrostatic potential using the following formula:

$$\bar{V}(z) = \frac{1}{ab} \int_{z-a/2}^{z+a/2} dz' \int_{z'-a/2}^{z'+b/2} V(z'') dz'', \quad (6)$$

where a and b are the lattice constants of Si and EuO, respectively. We will use this as our reference potential. The values for the reference potentials in the bulklike regions of Si and EuO are $\bar{V} = -3.33$ eV and $\bar{V} = +0.50$ eV, respectively. We can place the corresponding valence-band maxima (VBMs) using the shift values determined in two separate bulk calculations [red lines in Fig. 6(a)]. The energy difference between

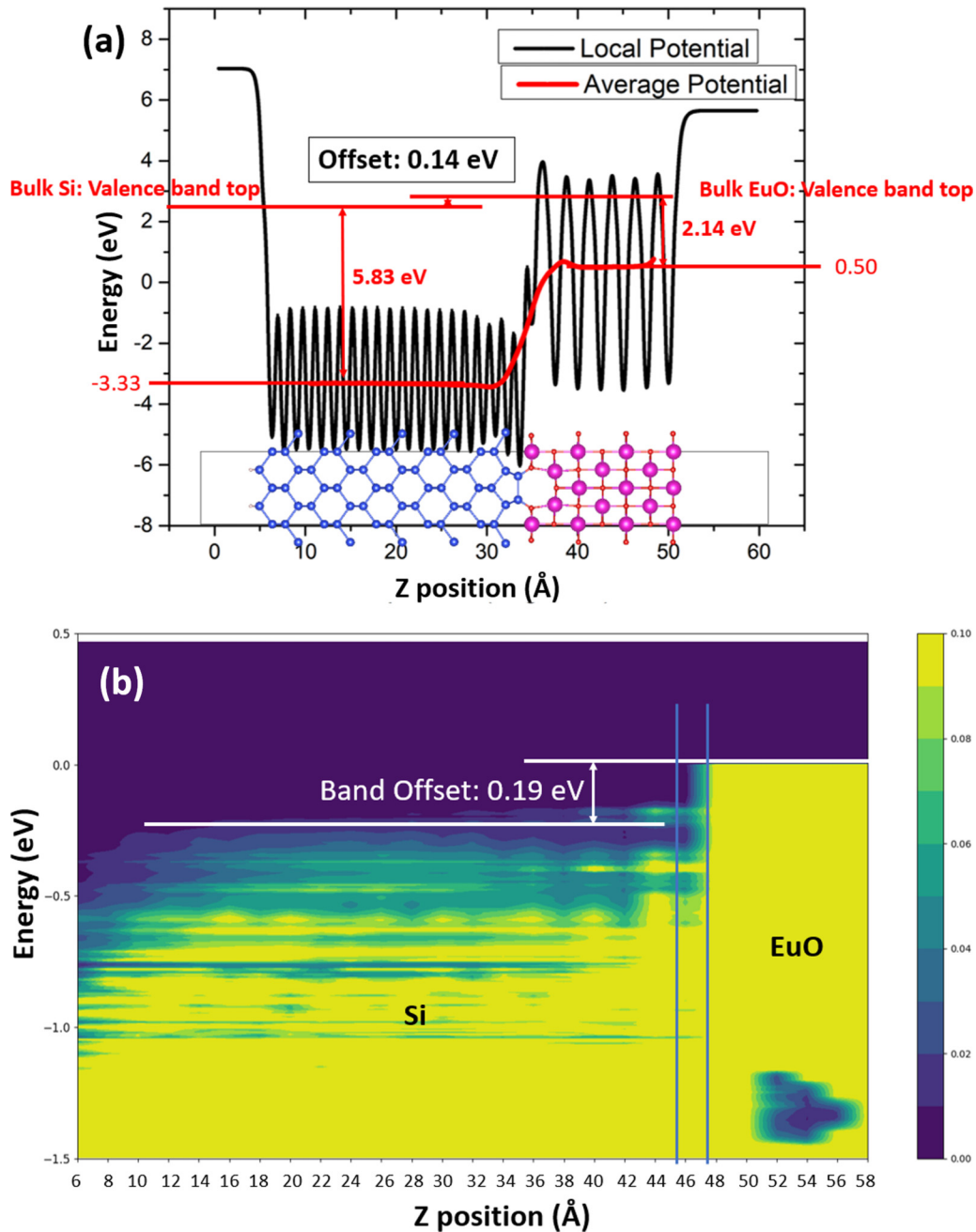


FIG. 6. (a) Average potential method of determining the VBO for interface model III. The z axis is the position in the direction normal to the interface. The black line represents the local electrostatic potential. The red line represents the average potential calculated using Eq. (6). The energy difference between the VBM and the average potential values of Si (5.83 eV) and EuO (2.14 eV) is used to determine the VBO of +0.14 eV. (b) Contour plot of PDOS for spin-up channel in the valence-band and band-gap regions (color map indicates DOS in arbitrary units). The dark blue region is the band gap and the yellow region is the valence-band top. White lines indicate the VBM of Si and EuO. Blue lines separate Si, EuO, and the interface area.

the VBM and the average potential is 5.83 and 2.14 eV in Si and EuO, respectively. We can then determine the VBO at the interface to be +0.14 eV (the EuO VBM is closer to vacuum). For the PDOS analysis, we make a contour plot of the PDOS as a function of energy and position along the z direction normal to the plane of the interface [Fig. 6(b)] with the color representing the DOS intensity. In the contour plot one can clearly see the band edges of Si and EuO and read off the VBO, which is +0.19 eV. In Table II, we summarize the

band offsets computed for all six interface models of Fig. 4 (positive means EuO VBM is closer to vacuum). The results from the APM and PDOS analysis are in good agreement with each other for all the interface models studied. As we have mentioned before, possible ferroelectricity in strained EuO may influence the CBO. However, based on Ref. [30], a 4.7% tensile strain in EuO results in a small ($\sim 5\text{-}\mu\text{C}/\text{cm}^2$) in-plane polarization (x and y direction), which does not directly influence the CBO in the out-of-plane direction (z direction).

TABLE II. Valence-band offsets computed for six interface models (see Fig. 3) using the average potential and projected density of states methods.

VBO (eV)	APM	PDOS analysis	VBO (eV)	APM	PDOS analysis
Interface model I	-0.80	-0.71	Interface model IV	-0.89	-0.80
Interface model II	-0.52	-0.50	Interface model V	-0.78	-0.74
Interface model III	+0.14	+0.18	Interface model VI	+0.12	+0.09

After complete atomic relaxation, we also observe an in-plane EuO displacement; however, it is antiferroelectric (AF). We attribute the stabilization of the AF distortion to interface reconstruction, caused by interaction with the Si dimer. The ferroelectric minimum is very shallow, and is easily overcome by the interface in a thin film considered here.

Core-level spectroscopy is a key technique when analyzing the chemistry and physics of a surface or interface; the core-level position reveals the local properties around an atom, such as oxidization, charge transfer, chemical bonding, etc. In our six interface models, due to the different interface oxidization levels, the Si $2p$ core level may have significant interface core-level shifts (ICLS) that can be detected by XPS. *Ab initio* theory can be used to predict ICLS. The relative position between the core level and vacuum level (binding energy) is given by $E_B = E(n_c - 1) - E(n_c)$. To simulate the XPS experiment, the ejected electron knocked out by x rays is placed in a valence or conduction band to maintain charge neutrality of the simulation cell, while leaving an electron core hole localized around the atom. We allow the surrounding electrons to screen the core hole, which is the so-called final-state theory [39,40]. Hence, the ICLS is

given by

$$E_{\text{ICLS}} = [E_{\text{interface}}(n_c - 1) - E_{\text{interface}}(n_c)] - [E_{\text{bulk}}(n_c - 1) - E_{\text{bulk}}(n_c)]. \quad (7)$$

We assume the atoms in the middle of the slab correspond to bulk Si. In Eq. (7), we make the following approximation: $E_{\text{interface}}(n_c) \approx E_{\text{bulk}}(n_c)$, and use this to calculate the Si $2p$ core-level shift of each atom relative to bulk Si.

The ICLS values for the first three layers of Si in interface model VI (we explain in the following section why we chose to calculate this interface model) are shown in Fig. 7 as vertical lines. These atoms, labeled as Si1, Si2, Si3, and Si4 in the inset of Fig. 7, have the largest shift from the bulk. For the Si atoms below the third layer, the ICLS values are very small and can be treated as bulk. We notice that for first-layer Si atoms (the dimer atoms), the ICLS value is -2.02 eV. A shoulder on the higher binding-energy side of the experimental XPS spectrum is consistent with this ICLS and has been traditionally interpreted as Si^{2+} oxidation state. This oxidation state is consistent with the Si-O bonding present in the fully oxidized interface model (VI).

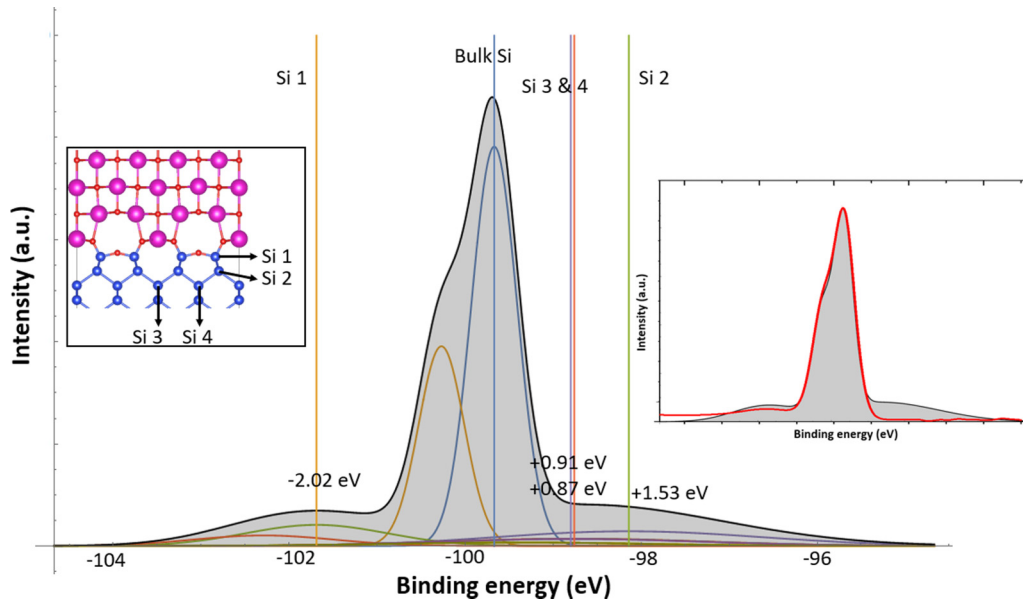


FIG. 7. *Ab initio* simulated Si $2p$ XPS spectrum. The relative binding energy is shifted based on the experimental value of the bulk binding energy of -99.67 eV. The ICLS values of four Si atoms are displayed and labeled by straight vertical lines (negative means deeper binding energy and positive means closer to vacuum). The peaks next to the main peaks (separated by 0.6 eV) are spin-orbit-split peaks with half intensity. We use a Gaussian shape to simulate the XPS signal. Black line and gray area are total XPS spectra. Color lines are Gaussians of each peak. The left panel indicates the position of each Si atom with a significant ICLS value. The rest of the Si atoms' ICLS are small and are considered the same as bulk. The inset panel on the right is a comparison between theory and experimental XPS spectra (red line is experimental data).

In order to construct a theoretical XPS spectrum, we place a Gaussian at each ICLS component (bulk, Si 1, Si 2, Si 3, and Si 4). To estimate the intensity of each peak, we first calculate the effective attenuation length for Si based on the CS-2 formula [41] and obtain a value of 2.91 nm. The effective attenuation length λ describes the exponential decay of the XPS signal $e^{-h/\lambda}$ (h is the depth of the atom with respect to the surface) as it propagates through the material to the surface. To simplify the calculation, we ignore the effective attenuation in EuO because it affects all Si photoelectrons equally. The number of Si atoms corresponding to the bulk, first, second, and third layers as well as how far below the interface they are located determine the intensity of each component. It is essential to point out that each component has a spin-orbit pair that has 0.6 eV higher binding energy and half the intensity. Figure 7 (black line and gray area) shows the predicted total XPS intensity from the Si atoms. The second inset on the right compares the theoretical prediction to the experimental XPS spectrum for the oxidized interface, which is described in more detail in the next section.

V. EXPERIMENTAL RESULTS

Experimental band offsets for the two methods of growing EuO on Si described above were measured using core-level peak positions of the 2.5-nm EuO/Si heterostructure, in combination with data for the valence-band maximum to core-level separation for single-crystal Si wafer and for 20-nm epitaxial EuO grown on yttria-stabilized zirconia. The measured core-level spectra of Eu $4d$ and Si $2p$ for the first growth method (oxygen first) is shown in Fig. 8(a). The Si $2p$ spectrum shows the 0.6-eV spin-split Si $2p$ level at a binding energy of 99.67 eV, with a small shoulder at 101.81 eV indicating the presence of partially oxidized silicon atoms at the interface. The bulk peak and partially oxidized Si (Si1) peak match the theoretical predictions well. The experimental XPS also has a low binding-energy component 0.63 eV lower than the bulk component. This is close to the Si3/Si4 components at 0.9 eV predicted by DFT. The experimental XPS, however, does not show the very low binding-energy Si2 component predicted by theory.

Figure 8(a) also shows the complex multiplet-split spectrum of Eu (II) $4d$ that is consistent with Eu^{2+} . The primary component of Eu $4d$ in the heterostructure has a binding energy of 129.19 eV. This means that the Eu $4d$ -Si $2p$ separation in the heterostructure is 29.52 eV. With the VBM-Si $2p$ separation of 98.89 eV in pure n -Si and VBM-Eu $4d$ separation of 128.52 eV in pure EuO, this yields a measured VBO for the oxygen-first growth method of 0.10 ± 0.10 eV. Figure 8(b) shows the Eu $4d$ and Si $2p$ spectra for the second growth pathway (metal first). No partially oxidized Si components are present in this case. The same analysis performed on this heterostructure yields a VBO of 0.35 ± 0.10 eV for the metal-first growth method.

VI. THEORY-EXPERIMENT COMPARISON AND DISCUSSION

The oxygen partial pressure during sample growth is 3×10^{-9} Torr, and the chemical potential of oxygen is

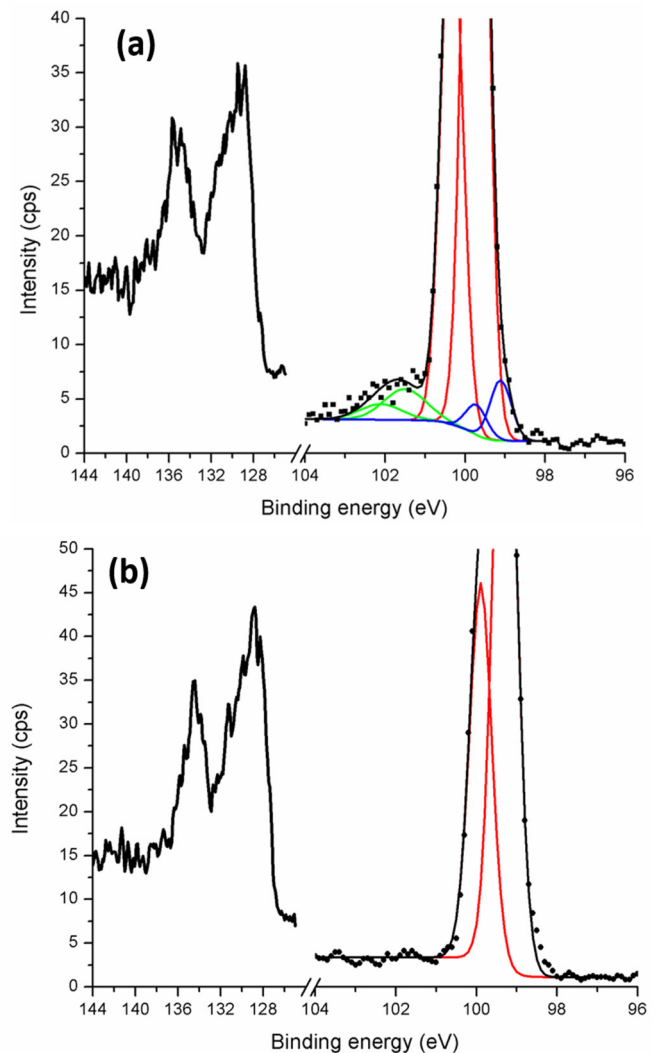


FIG. 8. X-ray photoemission spectra of the Si/EuO heterostructures grown using the two approaches mentioned in the main text. (a) Oxygen-first pathway. (b) Metal-first pathway.

given by

$$\mu_{\text{O}_2} = kT \left[\ln \left(\frac{pV_Q}{kT} \right) - \ln(Z_{\text{rot}}) - \ln(Z_{\text{vib}}) \right], \quad (8)$$

where k is the Boltzmann constant; p is pressure; $V_Q = (h^2/2\pi mkT)^{3/2}$ is the quantum volume; Z_{rot} and Z_{vib} are the rotational and vibrational partition functions of an oxygen molecule, respectively. We estimate the oxygen chemical potential corresponding to the growth pressure to be -2.57 eV. Then according to the stability phase diagram in Fig. 5(b), interface models V and VI are the most probable configurations at this oxygen chemical potential. Because the growth is Eu-limited, we are also in Eu-poor conditions and hence model VI is the most probable configuration based on experimental conditions and we mainly focus on this model in the subsequent discussion.

Starting with the 1/2 ML Zintl template, the sample is exposed to oxygen (3×10^{-9} Torr), which is sufficient to oxidize the bridge and to create decorating oxygen atoms on the Si surface. Subsequent deposition of Eu in the presence

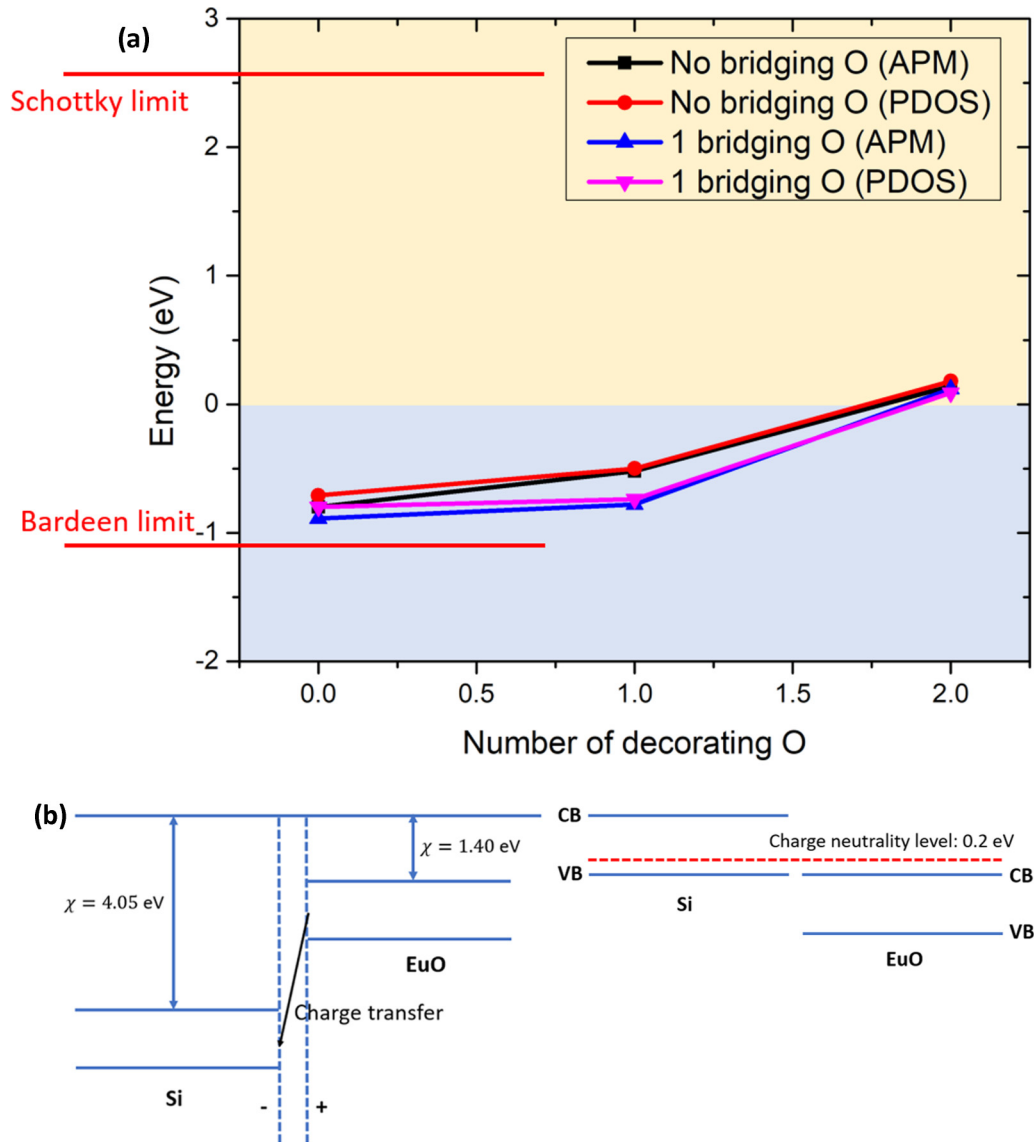


FIG. 9. (a) Plot of VBO versus number of d. oxygen and b. oxygen atoms via the APM and PDOS analysis. The blue area indicates where the Si VBM is higher than EuO VBM and the yellow area indicates where the EuO VBM is higher than the Si VBM. The two red horizontal line segments indicate the VBO in the Schottky and Bardeen limits. (b) Schematic diagram showing both the Schottky and Bardeen limits.

of this oxygen partial pressure oxidizes the incoming Eu flux and forms EuO on top of Si. This oxygen partial pressure is just sufficient to oxidize Eu to Eu^{2+} with only a small amount of residual oxygen left (Eu is the limiting reactant in EuO formation). This matches the Eu-poor but moderate-oxygen conditions of Fig. 5(b) (yellow area in the phase diagram). The Si $2p$ core-level spectrum in Fig. 8(a) confirms that some Si is indeed oxidized, which agrees well with the DFT spectrum in Fig. 7. The measured VBO of +0.10 eV matches the calculated value of both interface III (green) and VI (yellow). Considering both experimental growth conditions and the VBO value, we claim that model VI is the most likely structure for the first growth method (oxygen first). A previous study about BaO/Si [37] also suggests that more than 1 ML of oxygen atoms are involved, which is similar to our model VI with one extra bridging oxygen. On the other hand, the metal-first second growth method starts with a fully metallic Eu (or EuSi_2) surface and is likely in the Eu-rich regime with

1 ML Eu as the starting layer rather than the 1/2 ML Zintl layer. Such growth conditions are not among the six interface models studied in detail. The measured VBO of +0.35 eV also does not match any of the calculated interface models with 1/2 ML Eu as the starting layer.

As for the interface electronic structure, it can be seen from Table II that the VBO depends strongly on the number of oxygen atoms at the interface, particularly on the number of decorating oxygen atoms. To illustrate this point, in Fig. 9(a) we plot the valence-band offset as a function of number of decorating oxygen atoms. It is clear that as this number increases, so does the VBO. Finally, for a “fully oxidized” interface, the EuO VBM is higher than that of Si. On the other hand, if we keep the number of decorating oxygen atoms constant and increase the number of bridging oxygen atoms, the VBO decreases. The effect, however, is not as pronounced. These results suggest that the VBO is tunable by varying the number of oxygen atoms or the interface oxidation level,

TABLE III. Static and high-frequency component of the dielectric constant and interface pinning factor for six interface models.

Dielectric constant	Interface dipole correction derived ϵ_0		MIGS ϵ_∞ and S_ϕ		Dielectric constant	Interface dipole correction derived ϵ_0		MIGS ϵ_∞ and S_ϕ	
	APM	PDOS	APM	PDOS		APM	PDOS	APM	PDOS
Structure I	10.61	10.89	11.72, 0.08	10.28, 0.10	Structure IV	11.75	12.06	13.98, 0.06	11.72, 0.08
Structure II	11.12	11.19	8.39, 0.15	8.24, 0.16	Structure V	11.39	11.53	11.35, 0.09	10.70, 0.10
Structure III	11.26	11.44	5.50, 0.33	5.39, 0.34	Structure VI	13.88	13.72	5.55, 0.33	5.64, 0.32

i.e., by controlling the interface oxidization conditions from the experimental point of view.

In Fig. 9(a), we also indicate the VBOs predicted by the Schottky [42] and Bardeen [43] models. Our VBOs are closer to the Bardeen limit. However, interface oxidation can shift the VBO closer to the Schottky limit. In the Schottky limit, the electron affinities χ of EuO and Si are 1.40 eV [44] and 4.05 eV [45], respectively, placing the VBM of EuO 2.65 eV above the conduction band of Si based on $\phi = \chi_a - \chi_b$ [left panel of Fig. 9(b)]. In the Bardeen limit [right panel of Fig. 9(b)], it is assumed there is a continuous DOS across the gap filled up to a specific energy level called the charge-neutrality level (CNL) [46], with the band lineup given

by

$$\phi = (\chi_a - \phi_{\text{CNL},a}) - (\chi_b - \phi_{\text{CNL},b}),$$

where $\phi_{\text{CNL},a,b}$ indicates the energy difference between the CNL and the vacuum level. When Si (CNL 0.2 eV above VBM) and EuO (CNL 0.2 eV above conduction-band minimum (CBM) [46]) are brought into contact, their CNLs are aligned, giving a VBO of -1.1 eV.

One can also use the metal-induced gap states (MIGS) model [47–49]:

$$\phi = (\chi_a - \phi_{\text{CNL},a}) - (\chi_b - \phi_{\text{CNL},b}) + S_\phi(\phi_{\text{CNL},a} - \phi_{\text{CNL},b}), \quad (9)$$

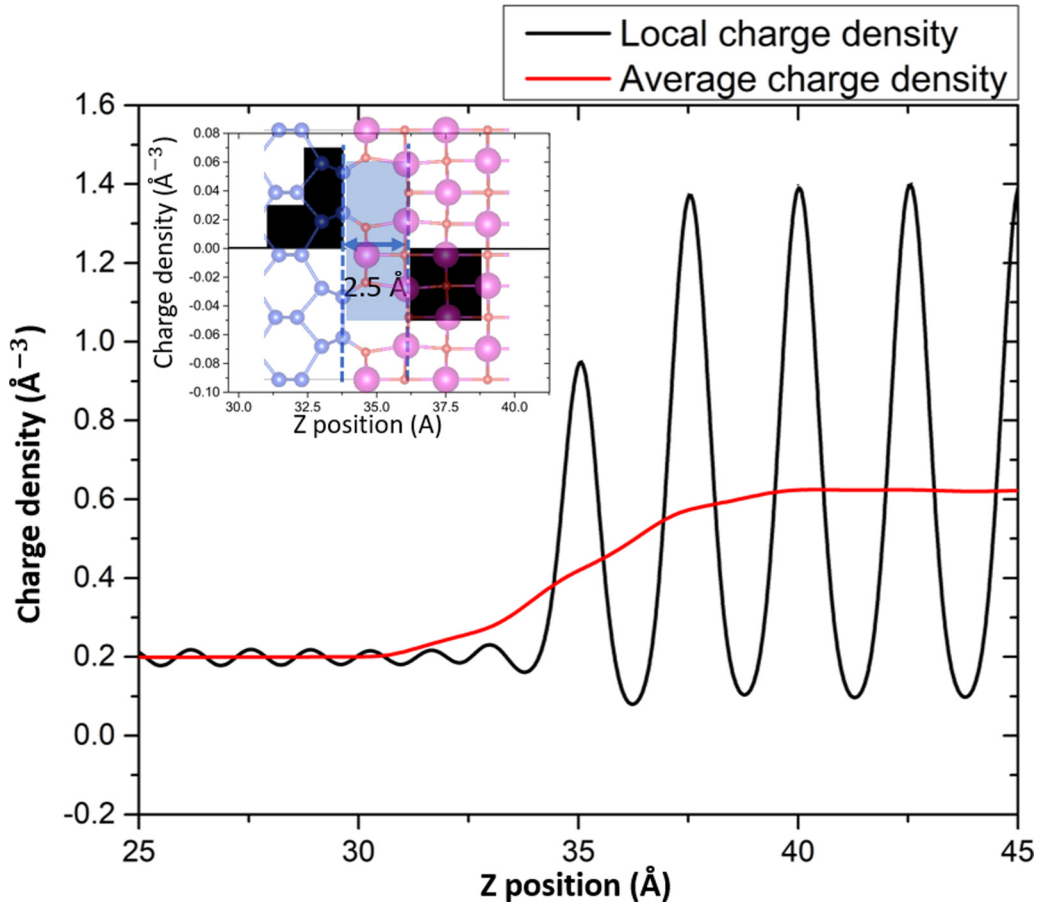


FIG. 10. Charge density around the interface. The black line represents the local charge density and the red line represents the average charge density via Eq. (6). Inset panel: Charge accumulation and depletion across the interface. The interface area is indicated by the light-blue background. The atomic structure of the interface is also shown. Blue dashed lines represent the plane capacitor model with the distance between the two planes being 2.5 \AA .

where S_ϕ is the pinning factor ($S_\phi = 0$ is Bardeen limit and $S_\phi = 1$ is Schottky limit),

$$S_\phi = \frac{1}{1 + 0.1(\epsilon_\infty - 1)^2}, \quad (10)$$

fitted from the experimental data [50], and ϵ_∞ is the high-frequency dielectric constant. Our VBOs fall in between the Bardeen and Schottky limits, which yields $0 < S_\phi < 1$, with oxidation reducing the pinning effect as discussed above. From Eqs. (8) and (9) and the computed values of VBOs, we can estimate the pinning factor S_ϕ and high-frequency dielectric constant for each interface region. The results are summarized in Table III.

The large energy difference between the CB of EuO and Si induces charge transfer from EuO to Si after they are placed in contact, creating the interface dipole as shown in the left panel of Fig. 9(b). We estimate the interface charge transfer and induced electrostatic energy shift for all six interface

models. Taking structure III as an example, we first plot the local charge density along the z direction of our simulation cell (black line in Fig. 10) and calculate the macroscopically averaged charge density [51] (red line in Fig. 10). To simplify the charge distribution, we approximate the charge density of each Si and EuO layer using constant values of average charge density at the center of each layer. We define the interface as the region between the first layer of Si and EuO. The interface defined as such is a multicomponent region with Si, EuO, O, and Eu Zintl layer, making it quite difficult to model the charge density by comparing with bulk. To simplify our interface model, we consider the interface region above as a combined chemical compound of Si, Eu, and O with a constant static dielectric constant. To calculate the energy shift, we approximate the interface as a parallel plate capacitor (indicated by the light-blue area and blue dashed lines in the inset panel of Fig. 10) [52]. We subtract from the charge density near the interface the average charge density of bulk

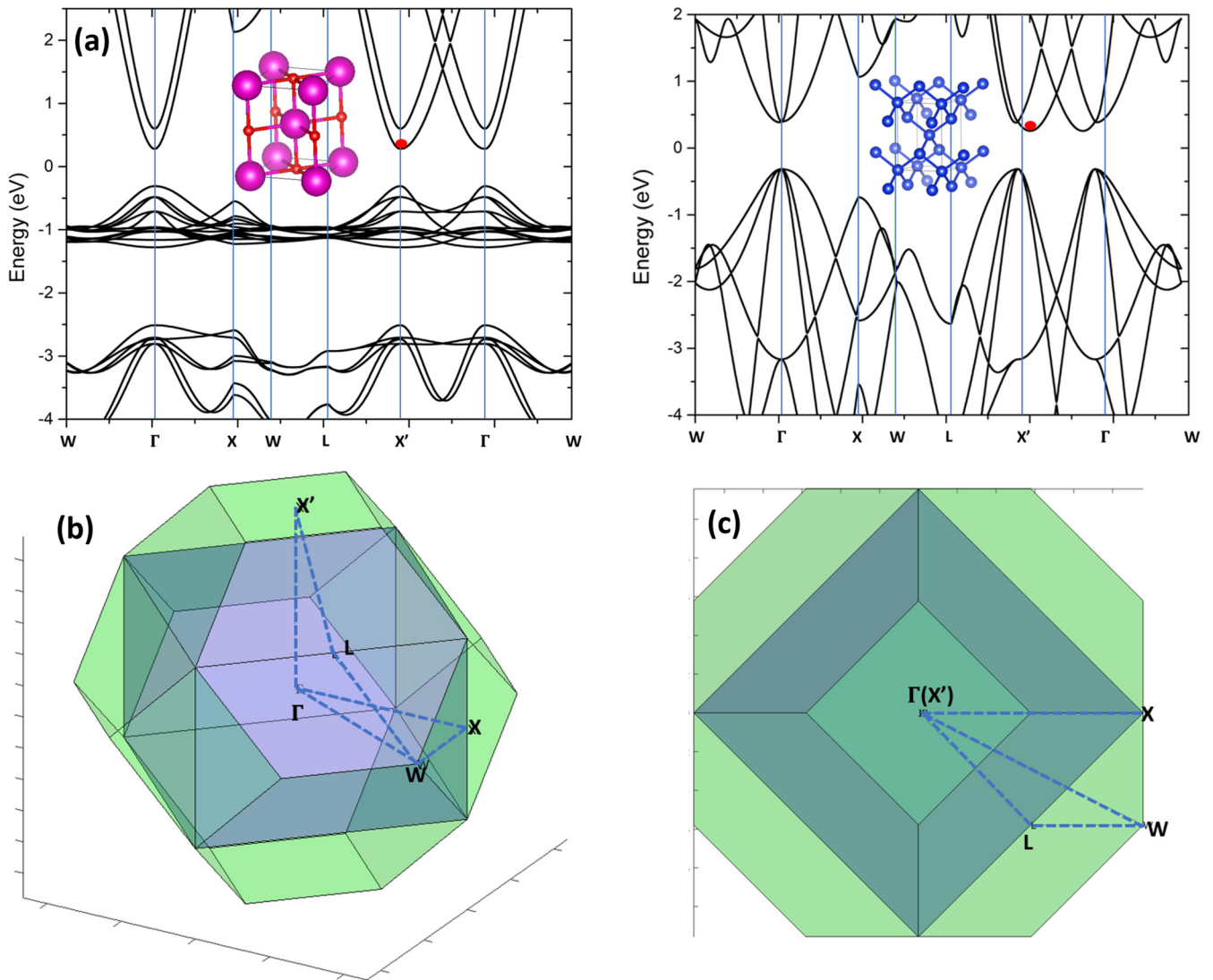


FIG. 11. (a) Band structure of EuO (left panel) and Si (right panel) tetragonal cells. Red dots indicate the conduction-band bottom. Inset panels show the simulation cells used. (b) First Brillouin zones of the face-centered cell (green) with high-symmetry points indicated and simple tetragonal cell (purple). Blue dashed lines represent band-structure plotting path. (c) Top view of the first Brillouin zones of fcc and tetragonal cells.

Si and EuO to derive the charge depletion and accumulation across the interface, as shown in the inset panel of Fig. 10. The energy shift of a parallel plate capacitor is $\Delta V = \frac{\rho d^2}{2\epsilon\epsilon_0}$, where ρ is the accumulated or depleted charge density near the interface ($0.05/\text{\AA}^3$ in our example), d is the thickness of the interface region (2.50\AA in our example), and ϵ is the effective dielectric constant of the interface. Thus, we can obtain the VBO with the energy correction due to the interface dipole,

$$\text{VBO} = V_{\text{Schottky}} - \frac{\rho d^2}{2\epsilon\epsilon_0} = 2.65 - \frac{28.25}{\epsilon} \text{ eV}. \quad (11)$$

We can use Eq. (11) to estimate the effective interface dielectric constant using the VBO from DFT. The static and high-frequency values of the dielectric constant are summarized in Table III.

To investigate the efficiency of spin injection across the Si/EuO interface, we consider the momentum of injected electrons in both the Si and EuO regions. Well-aligned momenta across the interface suggests a high injection efficiency. We plot the band structure of Si and strained EuO using a tetragonal cell as shown in Fig. 11(a) instead of the conventional fcc cell for convenience. The high-symmetry path in the first Brillouin zone is shown in Figs. 11(b) and 11(c). We use high-symmetry points defined in fcc cell and provide the mapping between these two Brillouin zones. The band-structure results are in good agreement with prior work [53]. Because of the spin splitting of the EuO $5d$ conduction band, the carriers that will be injected into the CBM of Si are expected to be 100% spin polarized.

The momenta at the CBM of Si and EuO are $(0, 0, 0.98)\text{\AA}^{-1}$ and $(0, 0, 1.27)\text{\AA}^{-1}$, respectively, and are aligned along the z direction, while their magnitudes differ slightly. This suggests only a limited amount of backscattering. From the band structure, we also calculate the effective mass at the CBM of Si and EuO. For Si, the longitudinal and transverse effective masses are $0.95m_e$ and $0.21m_e$, close to the theoretical values $0.98m_e$ and $0.19m_e$. For EuO, the

calculated longitudinal and transverse effective masses are $1.07m_e$ and $0.39m_e$. With the higher effective masses in EuO, if we tune the CBO such that the Si CBM is higher than that of EuO, or supply an external electric field to move electrons from Si back to EuO, it may be possible to observe a Gunn-like effect [54] in Si/EuO heterostructures, resulting in negative differential resistance that can be implemented in the design of oscillators.

VII. CONCLUSIONS

Using a combination of first-principles calculations and experiment, we study the atomic structure and band alignment of the Si/EuO interface. First, we establish that the most stable position of a Eu adatom on the dimerized Si surface is in the troughs between Si dimers, similar to what is known for Sr and Ba adatoms on the Si surface. This suggests that one may be able to transfer the experimental techniques developed for Sr and Ba when depositing Eu. Considering the interface stability, we find that as expected, the oxygen chemical potential controls the interface oxidation while the Eu chemical potential specifically controls oxidation of the dimer bridges. Theoretical and experimental core-level XPS spectra for the oxygen-first method agree with each other well and indicate that fully oxidized interface (model VI) is the most likely structure experimentally. The calculated interface phase diagram suggests a way to tune the interface oxidation and in turn, the band alignment between the two materials. The band alignment at the Si/EuO interface is closer to the Bardeen limit but shifts toward the Schottky limit as the interface oxidation is increased.

ACKNOWLEDGMENTS

We thank Lingyuan Gao for helpful discussions of EuO calculations, Ali Hamze for his help with XPS simulations, and Donghan Shin for his critical review of the manuscript. The work is supported by the Air Force Office of Scientific Research under Grant No. FA9550-18-1-0053.

-
- [1] S. Datta and B. Das, *Appl. Phys. Lett.* **56**, 665 (1990).
 [2] R. A. McKee, F. J. Walker, and M. F. Chisholm, *Phys. Rev. Lett.* **81**, 3014 (1998).
 [3] G. Schmidt, D. Ferrand, L. W. Molenkamp, A. T. Filip, and B. J. van Wees, *Phys. Rev. B* **62**, R4790 (2000).
 [4] B.C. Min, K. Motohashi, C. Lodder, and R. Jansen, *Nat. Mater.* **5**, 817 (2006).
 [5] A. Schmehl *et al.*, *Nat. Mater.* **6**, 882 (2007).
 [6] B. T. Matthias, R. M. Bozorth, and J. H. Van Vleck, *Phys. Rev. Lett.* **7**, 160 (1961).
 [7] V.-C. Lee and L. Liu, *Phys. Rev. B* **30**, 2026 (1984).
 [8] J. Lettieri, V. Vaithyanathan, S. K. Eah, J. Stephens, V. Sih, D. D. Awschalom, J. Levy, and D. G. Schlom, *Appl. Phys. Lett.* **83**, 975 (2003).
 [9] N. Jutong, U. Eckern, T. Mairoser, and U. Schwingenschlogl, *Sci. Rep.* **5**, 8038 (2015).
 [10] I. Zutic, J. Fabian, and S. Sarma, *Rev. Mod. Phys.* **76**, 323 (2004).
 [11] D. Averyanov, Y. Sadofyev, A. Tokmachev, A. Primenko, I. Likhachev, and V. Storchak, *ACS Appl. Mater. Interfaces* **7**, 6146 (2015).
 [12] D. Averyanov, C. Karateeva, I. Karateev, A. Tokmachev, A. Vasiliev, S. Zolotarev, I. Likhachev, and V. Storchak, *Sci. Rep.* **6**, 22841 (2016).
 [13] D. Averyanov, C. Karateeva, I. Karateev, A. Tokmachev, M. Kuzmin, P. Laukkanen, A. Vasiliev, and V. Storchak, *Mater. Des.* **116**, 616 (2017).
 [14] L. Lev, D. Averyanov, A. Tokmachev, F. Bisti, V. Rogalev, V. Strocov, and V. Storchak, *J. Mater. Chem. C* **5**, 192 (2017).
 [15] J. Mundy, D. Hodash, A. Melville, R. Held, T. Mairoser, D. Muller, L. Kourkoutis, A. Schmehl, and D. Schlom, *Appl. Phys. Lett.* **104**, 091601 (2014).
 [16] C. Caspers, M. Müller, A. X. Gray, A. M. Kaiser, A. Gloskovskii, C. S. Fadley, W. Drube, and C. M. Schneider, *Phys. Status Solidi (RRL)* **5**, 441 (2011).

- [17] C. Caspers, M. Müller, A. X. Gray, A. M. Kaiser, A. Gloskovskii, C. S. Fadley, W. Drube, and C. M. Schneider, *Phys. Rev. B* **84**, 205217 (2011).
- [18] C. Caspers, A. Gloskovskii, M. Gorgoi, C. Besson, M. Luysberg, K. Z. Rushchanskii, M. Ležaić, C. S. Fadley, W. Drube, and M. Müller, *Sci. Rep.* **6**, 22912 (2016).
- [19] C. Caspers, S. Flade, M. Gorgoi, A. Gloskovskii, W. Drube, C. M. Schneider, and M. Müller, *J. Appl. Phys.* **113**, 17C505 (2013).
- [20] A. A. Demkov, H. Seo, X. Zhang, and J. Ramdani, *Appl. Phys. Lett.* **100**, 071602 (2012).
- [21] A. Slepko and A. A. Demkov, *Phys. Rev. B* **85**, 195462 (2012).
- [22] M. Choi, A. B. Posadas, H. Seo, R. C. Hatch, and A. A. Demkov, *Appl. Phys. Lett.* **102**, 031604 (2013).
- [23] K. D. Fredrickson, H. Seo, and A. A. Demkov, *J. Appl. Phys.* **120**, 065301 (2016).
- [24] G. Kresse and J. Furthmüller, *Phys. Rev. B* **54**, 11169 (1996).
- [25] J. P. Perdew, K. Burke, and M. Ernzerhof, *Phys. Rev. Lett.* **77**, 3865 (1996).
- [26] P. E. Blöchl, *Phys. Rev. B* **50**, 17953 (1994).
- [27] J. Lee, N. Sai, and A. A. Demkov, *Phys. Rev. B* **82**, 235305 (2010).
- [28] L. Gao and A. A. Demkov, *Phys. Rev. B* **97**, 125305 (2018).
- [29] N. J. C. Ingle and I. S. Elfimov, *Phys. Rev. B* **77**, 121202(R) (2008).
- [30] E. Bousquet, N. A. Spaldin, and P. Ghosez, *Phys. Rev. Lett.* **104**, 037601 (2010).
- [31] K. D. Fredrickson, P. Ponath, A. B. Posadas, M. R. McCartney, T. Aoki, D. J. Smith, and A. A. Demkov, *Appl. Phys. Lett.* **104**, 242908 (2014).
- [32] J. W. Reiner and Y. Segal, *J. Vac. Sci. Technol.* **27**, 2015 (2009).
- [33] R. Mckee, F. Walker, M. B. Nardelli, W. A. Shelton, and G. M. Stocks, *Science* **300**, 1726 (2003).
- [34] G. Henkelman and H. Jónsson, *J. Chem. Phys.* **113**, 9901 (2000).
- [35] J. Wang, J. A. Hallmark, D. S. Marshall, W. J. Ooms, P. Ordejón, J. Junquera, D. Sánchez-Portal, E. Artacho, and J. M. Soler, *Phys. Rev. B* **60**, 4968 (1999).
- [36] Y. Segal, J. W. Reiner, A. M. Kolpak, Z. Zhang, S. Ismail-Beigi, C. H. Ahn, and F. J. Walker, *Phys. Rev. Lett.* **102**, 116101 (2009).
- [37] M. Kuzmin, P. Laukkanen, M. P. J. Punkkinen, M. Yasir, M. Tuominen, J. Dahl, J. J. K. Lång, J. Mäkelä, and K. Kokko, *Phys. Rev. B* **90**, 235405 (2014).
- [38] L. Kleinman, *Phys. Rev. B* **24**, 7412 (1981).
- [39] L. Kohler and G. Kresse, *Phys. Rev. B* **70**, 165405 (2004).
- [40] E. Pehlke and M. Scheffler, *Phys. Rev. Lett.* **71**, 2338 (1993).
- [41] P. Cumpson and M. Seah, *Surf. Interface Anal.* **25**, 430 (1997).
- [42] W. Schottky, *Z. Phys.* **118**, 539 (1942).
- [43] J. Bardeen, *Phys. Rev.* **71**, 717 (1947).
- [44] K. Fredrickson and A. A. Demkov, *J. Appl. Phys.* **119**, 095309 (2016).
- [45] S. M. Sze, *Physics of Semiconductor Devices* (Wiley, New York, 1981).
- [46] W. Heine, *Phys. Rev.* **138**, A1689 (1965).
- [47] J. Tersoff, *Phys. Rev. Lett.* **52**, 465 (1984).
- [48] J. Robertson, *J. Vac. Sci. Technol. B* **18**, 1785 (2000).
- [49] C. Tejedor, F. Flores, and E. Louis, *J. Phys. C: Solid State Phys.* **10**, 2163 (1977).
- [50] W. Mönch, *Surf. Sci.* **299–300**, 928 (1994).
- [51] A. Baldereschi, S. Baroni, and R. Resta, *Phys. Rev. Lett.* **61**, 734 (1988).
- [52] O. Sharia, A. A. Demkov, G. Bersuker, and B. H. Lee, *Phys. Rev. B* **75**, 035306 (2007).
- [53] N. Jutong, I. Rungger, C. Schuster, U. Eckern, S. Sanvito, and U. Schwingenschlögl, *Phys. Rev. B* **86**, 205310 (2012).
- [54] J. B. Gunn, *Solid State Commun.* **1**, 88 (1963).